

## Surface area overestimation within three-dimensional digital images and its consequence for skeletal dosimetry

D. A. Rajon, P. W. Patton, A. P. Shah, C. J. Watchman, and W. E. Bolch

Citation: *Medical Physics* **29**, 682 (2002); doi: 10.1118/1.1470207

View online: <http://dx.doi.org/10.1118/1.1470207>

View Table of Contents: <http://scitation.aip.org/content/aapm/journal/medphys/29/5?ver=pdfcov>

Published by the [American Association of Physicists in Medicine](#)

### Articles you may be interested in

Three dosimetry models of lipoma arborescens treated by 90Y synovectomy

Med. Phys. **41**, 052501 (2014); 10.1118/1.4870382

Skeletal dosimetry for external exposures to photons based on  $\mu$  CT images of spongiosa: Consideration of voxel resolution, cluster size, and medullary bone surfaces

Med. Phys. **36**, 5007 (2009); 10.1118/1.3242266

X-band EPR imaging as a tool for gradient dose reconstruction in irradiated bones

Med. Phys. **36**, 4223 (2009); 10.1118/1.3194775


A study of multi-modality imaging for three-dimensional radiotherapy treatment planning of brain tumors

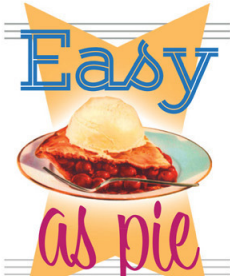
Med. Phys. **31**, 685 (2004); 10.1118/1.1645631

Magnetic resonance imaging based digitally reconstructed radiographs, virtual simulation, and three-dimensional treatment planning for brain neoplasms

Med. Phys. **25**, 1928 (1998); 10.1118/1.598382

Read the full article online for free at





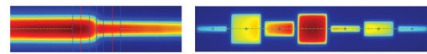
**Easy**  
**as pie**

**RITG148<sup>+</sup>**

*Custom Designed*

**TG-148 Tests**

*For Tomotherapy QA*




RIT is your only source for the tests specified for helical tomotherapy in the TG-148 report. These automated QA tests include:

• Automated QA testing	• MLC alignment test
• Y-jaw divergence/beam centering	• Couch translation/gantry rotation
• Y-jaw/gantry rotation plane alignment	• Laser localization
• Gantry angle consistency	• Image quality tests (Cheese Phantom)
• Treatment field centering	• Built in trending and reporting with RITrend

These tests are included in both our RITComplete, and RITG148+ products.

Call 719.590.1077,  
option 4, or email  
[mac@radimage.com](mailto:mac@radimage.com)  
today to set up your  
personal demo.



# Surface area overestimation within three-dimensional digital images and its consequence for skeletal dosimetry

D. A. Rajon

*Department of Nuclear and Radiological Engineering, University of Florida, Gainesville, Florida 32611-8300*

P. W. Patton

*Department of Health Physics, University of Nevada—Las Vegas, Las Vegas, Nevada 89154-3037*

A. P. Shah, C. J. Watchman, and W. E. Bolch<sup>a)</sup>

*Department of Nuclear and Radiological Engineering, University of Florida, Gainesville, Florida 32611-8300*

(Received 31 July 2001; accepted for publication 8 February 2002; published 10 April 2002)

The most recent methods for trabecular bone dosimetry are based on Monte Carlo transport simulations within three-dimensional (3D) images of real human bone samples. Nuclear magnetic resonance and micro-computed tomography have been commonly used as imaging tools for studying trabecular microstructure. In order to evaluate the accuracy of these techniques for radiation dosimetry, a previous study was conducted that showed an overestimate in the absorbed fraction of energy for low-energy electrons emitted within the marrow space and irradiating the bone trabeculae. This problem was found to be related to an overestimate of the surface area of the true bone-marrow interface within the 3D digital images, and was identified as the surface-area effect. The goal of the present study is to better understand how this surface-area effect occurs in the case of single spheres representing individual marrow cavities within trabecular bone. First, a theoretical study was conducted which showed that voxelization of the spherical marrow cavity results in a 50% overestimation of the spherical surface area. Moreover, this overestimation cannot be reduced through a reduction in the voxel size (e.g., improved image resolution). Second, a series of single-sphere marrow cavity models was created with electron sources simulated within the sphere (marrow source) and outside the sphere (bone trabeculae source). The series of single-sphere models was then voxelized to represent 3D digital images of varying resolution. Transport calculations were made for both marrow and bone electron sources within these simulated images. The study showed that for low-energy electrons ( $<100$  keV), the 50% overestimate of the bone-marrow interface surface area can lead to a 50% overestimate of the cross-absorbed fraction. It is concluded that while improved resolution will not reduce the surface area effects found within 3D image-based transport models, a tenfold improvement in current image resolution would compensate the associated errors in cross-region absorbed fractions for low-energy electron sources. Alternatively, other methods of defining the bone-marrow interface, such as with a polygonal isosurface, would provide improvements in dosimetry without the need for drastic reductions in image voxel size. © 2002 American Association of Physicists in Medicine. [DOI: 10.1118/1.1470207]

Key words: trabecular bone, voxel effects, NMR microscopy, marrow dosimetry, 3D surface

## I. INTRODUCTION

Trabecular bone is that portion of the adult human skeleton which houses the hematopoietic marrow, the tissue responsible for the production of various blood cells. The high mitotic activity of active bone marrow thus makes this organ one of high radiation sensitivity, and is thus of high interest in the dosimetry of radionuclide therapies where marrow toxicity is generally dose-limiting.<sup>1,2</sup> Internal irradiation of bone marrow may result from occupational exposures to bone-seeking radionuclides,<sup>3</sup> radionuclide therapy of tumors,<sup>4</sup> and bone pain palliation treatments.<sup>5</sup> In these different situations, the absorbed dose to the bone marrow results from both the physical aspects of the radiation transport and energy deposition, as well as the biological aspects that determine source location and the cumulative number of

nuclear decays. In regard to the physical aspects of skeletal dosimetry, the microstructural complexity of trabecular bone<sup>6,7</sup> imposes challenges to the construction of dosimetry models of this skeletal region, particularly as needed to assess absorbed fractions of energy for electron sources.

### A. Bone marrow dosimetry

Bone marrow dosimetry has been investigated extensively during the past 40 years. During the 1960s to early 1970s, Spiers and colleagues conducted the first comprehensive studies in skeletal dosimetry at the University of Leeds.<sup>8–14</sup> Following the establishment of a reference man skeletal model, other investigators have expanded these techniques to permit dose estimation specific to medical internal dosimetry.<sup>15–21</sup> Nevertheless, the complexity of the bone mi-

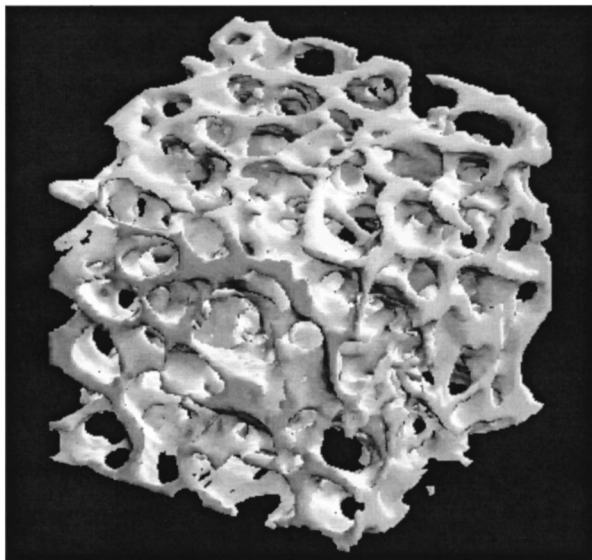


FIG. 1. A reconstruction of a 3D NMR image of a cubical sample of trabecular bone obtained at 4.7 T. The sample was sectioned from the right femoral head of a 51-year male. The sample size is  $5.6 \times 5.6 \times 5.6 \text{ mm}^3$ . The image resolution is  $88 \times 88 \times 88 \text{ } \mu\text{m}^3$ .

crostructure and its variations with patient age<sup>22–25</sup> have made it difficult to define models for bone marrow dosimetry that provide improved patient specificity over the single reference model for the adult male. During the 1990s, several groups have investigated the use of three-dimensional (3D) imaging techniques such as micro-computed tomography (microCT) and nuclear magnetic resonance (NMR) imaging to acquire 3D digital images of trabecular bone samples. These techniques have been used to measure regional bone mineral density and structural parameters.<sup>26–40</sup> Recently, NMR microscopy has been applied to the study of skeletal dosimetry.<sup>41–44</sup> This technique uses high-field NMR spectrometers to acquire high-resolution ( $\sim 60\text{--}90 \text{ } \mu\text{m}$ ) 3D images of trabecular bone. The images are then directly coupled to Monte Carlo radiation transport codes to calculate the deposition of energy by monoenergetic electrons within bone marrow. The code used is EGS4-PRESTA as it allows voxelized geometry containing millions of voxels. Figure 1 shows a reconstruction of a 3D NMR image of a trabecular bone sample. On this image, the average thickness of the bone trabeculae is  $\sim 300 \text{ } \mu\text{m}$  and the average size of the marrow cavities is  $\sim 1000 \text{ } \mu\text{m}$ .

## B. Voxelization effects in bone marrow dosimetry

A 3D image is a digital representation of a real object. In the case of trabecular bone, two media are present within the image: the bone trabeculae and the marrow cavities. In the digital image, each voxel is assigned to bone or to marrow by image thresholding and segmentation.<sup>41</sup> Consequently, the interface between the two media, which is most likely a curved surface in the real bone sample, appears as a jagged surface in the 3D digital image due to the rectangular shape of the voxels. As a consequence, a 3D digital image is not a totally faithful representation of the real sample.<sup>45</sup> This prob-

lem has already been studied for chord length distributions within NMR images of trabecular bone<sup>42</sup> and has been defined by what the author calls pixel (or voxel) effects A and B. Both pixel effects A and B are a consequence of the rectangular shape of the voxels [or pixels in two-dimensional (2D) geometry]. Pixel effect A creates some sharp spikes over the entire chord-length distribution, whereas pixel effect B overestimates the amount of short chord lengths within the geometry. Pixel effect B thus contributes to an underestimation of the mean of the chord-length distribution.

For calculations of energy deposition, the 3D digital image is subsequently coupled to a Monte Carlo radiation transport code. Consequently, voxel effects are also expected to result in dosimetry errors when radiation particles are transported close to the bone-marrow interface. To evaluate the magnitude of these voxelization effects, a theoretical study was conducted by Rajon *et al.* using a mathematical model of trabecular bone.<sup>44</sup> The model was constructed of nonuniformly sized spheres representing marrow cavities, with the intervening spaces representing the bone trabeculae. The experiment involved (1) coupling the mathematical bone model with the radiation transport code EGS4, (2) simulating 3D imaging of the bone model through its voxelization at various degrees of image resolution, (3) coupling these voxelized images within EGS4, and (4) comparing the dosimetry results with and without image voxelization. The study permitted the identification of three voxel effects.

First, a geometry effect occurs when a particle travels parallel to the bone-marrow interface and deposits its energy alternatively within bone and marrow as a direct result of the jagged representation of the interface. This effect overestimates or underestimates the absorbed fraction to marrow tissues depending upon which side of the true interface the particle is traveling (marrow or bone). These errors were shown to cancel when the particle transport is averaged across the entire image.

Second, a volume effect is seen to overestimate the volume fraction of marrow at large voxel sizes. Below  $300 \text{ } \mu\text{m}$ , however, the error in the marrow volume fraction becomes insignificant and without consequence for the dose calculation.

The third effect is a surface-area effect. Due to the voxelization of the image, the surface area of the bone-marrow interface is not respected. Measurements within the mathematical bone model show that the total surface area throughout the entire image increases continuously from near zero at poor resolutions to a convergence value at high resolution.<sup>44</sup> Unfortunately, the convergence value is 50% higher than the true surface area within the mathematical model of trabecular bone. This overestimation has important consequences when the electron range is small compared to the voxel size. In this situation, the cross-absorbed fraction (e.g., a marrow source irradiating bone, or a bone source irradiating marrow) can also be overestimated by up to 50%. According to the study, for some low-energy beta emitters used for skeletal dosimetry, this effect can lead to a 25% overestimation of the cross-region absorbed dose.

The purpose of the present study is to give a scientific

TABLE I. Characteristics of the eight single-sphere models covering a typical range of bone marrow cavity sizes. The name of each model is the radius of the sphere in micrometers, rounded to the closest integer. The volume fraction represents the fraction of the cube that is contained within the marrow sphere.

Model name	Sphere radius ( $\mu\text{m}$ )	Cube size ( $\mu\text{m}$ )	Sphere surface area ( $\text{cm}^2$ )	Sphere volume ( $\text{cm}^3$ )	Volume fraction (%)
1400	1400.085 909	3072	$2.463 \times 10^{-1}$	$1.150 \times 10^{-2}$	39.65
1016	1016.085 909	2304	$1.297 \times 10^{-1}$	$4.394 \times 10^{-3}$	35.92
0728	728.085 909	1728	$6.662 \times 10^{-2}$	$1.617 \times 10^{-3}$	31.33
0512	512.085 909	1296	$3.295 \times 10^{-2}$	$5.625 \times 10^{-4}$	25.84
0350	350.085 909	972	$1.540 \times 10^{-2}$	$1.797 \times 10^{-4}$	19.57
0228	228.085 909	728	$6.537 \times 10^{-3}$	$4.970 \times 10^{-5}$	12.88
0137	137.085 909	546	$2.362 \times 10^{-3}$	$1.079 \times 10^{-5}$	6.62
0069	69.085 909	410	$5.998 \times 10^{-4}$	$1.381 \times 10^{-6}$	2.00

explanation for the bone-marrow interface overestimation, and its consequence on absorbed fraction calculations. The mathematical bone model developed for the previous study<sup>44</sup> was made of thousands of spheres uniformly distributed throughout a cube representing a sectioned piece of trabecular bone. To understand how it is possible that the surface area of the bone-marrow interface, when measured through a voxelized image, converges to a value different from its true value, a separate study is presented here with models representing isolated marrow-cavity spheres. In the text which follows, the previous model will be referred as the mathematical trabecular-bone model, whereas the models developed in the present study will be referred as single-sphere models.

## II. MATERIALS AND METHODS

### A. Construction of the 3D segmented images of the single-sphere models

A set of eight models was created in which a single sphere was located at the center of a cube representing a small trabecular bone sample encompassing a single marrow cavity. The radius of the sphere and the size of the cube were selected according to the following criteria: (1) the entire set should cover the range of typical marrow cavity sizes found in trabecular bone; (2) the series of cube sizes and sphere radii should follow approximately a geometric progression; (3) in each model, the sphere should be surrounded by a typical trabecular thickness; and (4) the sphere radius should be chosen so that it does not represent an integer number of voxels. The last condition ensures that the bone-marrow interface is rarely adjacent to a voxel side. Such an undesirable situation could introduce geometrical effects that could alter the results since it is never realized within a real bone sample where the marrow cavities are randomly located. Table I contains the characteristics of the series of single-sphere models. The ten digits of the sphere radius guarantees condition (4) defined previously.

Once the single-sphere models are defined, a grid structure is placed over the cubes, representing the voxel dimensions of a 3D image acquisition. Different voxel sizes are used for each model in order to cover the largest possible range of image resolution. The minimum voxel size is set to

$2.5 \mu\text{m}$ , which corresponds to the range of a 10 keV electron in bone marrow and of a 15 keV electron in cortical bone. The maximum voxel size is set so that each image contains at least one voxel of each media. Table II lists the voxel sizes used for the study. A geometric progression is also used for the choice of the number of voxels per dimension.

The segmentation of the different images into bone and marrow voxels is based upon a technique similar to that developed for the mathematical bone model.<sup>44</sup> The principle is to calculate the volume fraction of each voxel inside the sphere. If this volume fraction exceeds 0.5, the voxel is assigned to marrow; otherwise, it is assigned to bone. When the volume fraction is not easy to calculate analytically, a Monte Carlo sampling technique is used. Once the segmentation is complete, a compression technique similar to that developed for the mathematical bone model<sup>44</sup> is used which permits images as large as two billion voxels to be handled by the EGS4 transport code.

### B. Volume fraction occupied by the sphere within the segmented images

The previous study by Rajon *et al.*<sup>44</sup> showed that the volume fraction of marrow is not represented well for voxel sizes larger than  $300 \mu\text{m}$ . In order to verify this result, and to include its consequences in the data interpretation of the present study, a computer program was created to calculate the marrow volume fraction in the voxelized single-sphere models.

### C. Theoretical surface area of a voxelized sphere

As the resolution of a 3D image is improved, it would appear that the voxelized surface of the image would approach the exact surface of the real object. Nevertheless, the voxelized surface still follows rectangular shapes and the area measured within the 3D image does not converge to the real surface area, even though the voxel size is reduced to an infinitely small value. The problem is demonstrated in 2D as follows.

Consider a circle of radius  $R$  as shown in Fig. 2. If a 2D image of the circle is made with a digital imaging system, the result will be the grid structure shown in Fig. 2. For this example, let us assume that the imaging system assigns each



TABLE II. Voxel sizes for the different 3D images of the single-sphere models. The first column lists the image series with the image number representing the number of voxels per dimension. For example, image 4 is a 3D image  $4 \times 4 \times 4$  voxels in size. Each of the eight other columns represents a single-sphere model as defined in Table I. The data in each column give the voxel size of each 3D image of each single-sphere model. For example, image 124 of model 0728 (the cube size and the exact radius are found in Table I) has an image voxel size of  $13.94 \mu\text{m}$ . Image 4 of the model 0069 does not exist as its 64 voxels are all assigned to bone resulting from the small size of the marrow sphere it contains.

Image number	Model Name (sphere radius in $\mu\text{m}$ )							
	1400	1016	0728	0512	0350	0228	0137	0069
4	768.0	576.0	432.0	324.0	243.0	182.0	136.5	...
6	512.0	384.0	288.0	216.0	162.0	121.3	91.00	68.33
8	384.0	288.0	216.0	162.0	121.5	91.00	68.25	51.25
10	307.2	230.4	172.8	129.6	97.20	72.80	54.60	41.00
12	256.0	192.0	144.0	108.0	81.00	60.67	45.50	34.17
16	192.0	144.0	108.0	81.00	60.75	45.50	34.13	25.63
22	139.6	104.7	78.55	58.91	44.18	33.09	24.82	18.64
32	102.4	76.80	57.60	43.20	32.40	24.27	18.20	13.67
40	76.80	57.60	43.20	32.40	24.30	18.20	13.65	10.25
52	59.08	44.31	33.23	24.92	18.69	14.00	10.50	7.885
70	43.89	32.91	24.69	18.51	13.89	10.40	7.800	5.857
92	33.39	25.04	18.78	14.09	10.57	7.913	5.935	4.457
124	24.77	18.58	13.94	10.45	7.839	5.871	4.403	3.306
164	18.73	14.05	10.54	7.902	5.927	4.439	3.329	2.500
218	14.09	10.57	7.927	5.945	4.459	3.339	2.505	...
292	10.52	7.890	5.918	4.438	3.329	2.493	...	...
388	7.918	5.938	4.454	3.340	2.505	...	...	...
518	5.931	4.448	3.336	2.502	...	...	...	...
692	4.439	3.329	2.497	...	...	...	...	...
922	3.332	2.499	...	...	...	...	...	...
1228	2.502	...	...	...	...	...	...	...

pixel as dark or white according to the fraction of its surface that is outside or inside the circle. The white pixels will then represent the interior of the circle (marrow) and the dark pixels will represent the exterior (bone). Therefore, the perimeter of the circle, if measured within the image, is equal to the length of the cumulative interface between the white

pixels and the dark pixels. Each pixel side that belongs to this perimeter can be moved as shown by the arrows in order to form the large dashed square. Therefore, the perimeter of the voxelized circle is equal to the perimeter of the dashed square. The size of this square depends on the pixel size and can be slightly smaller or slightly larger than the diameter of the circle. When the pixel size is reduced to an infinitely small value, the size of the square converges to the diameter of the circle. The total perimeter of the image of the circle is therefore equal to eight times the radius of the circle. This, if compared with the exact perimeter of the circle, corresponds to an overestimate equal to

$$\frac{8R - 2\pi R}{2\pi R} = 0.2732 \Rightarrow 27.32\% . \quad (1)$$

This overestimate is the limit of convergence when the pixel size is reduced to an infinitely small value. For a larger pixel size, the overestimate will be slightly smaller or slightly larger than the convergence value. This variation about the convergence value results from the fact that, depending on the ratio between the circle radius and the pixel size, the circle will not exactly fit within the larger dashed square.

The 3D problem is more complex and can be solved analytically. A sphere of radius  $R$  can be considered as a set of slices along the  $z$  axis. Each slice is a flat disk with radius  $r$  varying with the distance  $z$ . This is represented in Fig. 3 where a 2D projection of the sliced sphere is shown. The vertical rectangles represent the disks seen on edge. The thickness  $dz$  of the disks is assumed to be the voxel size of

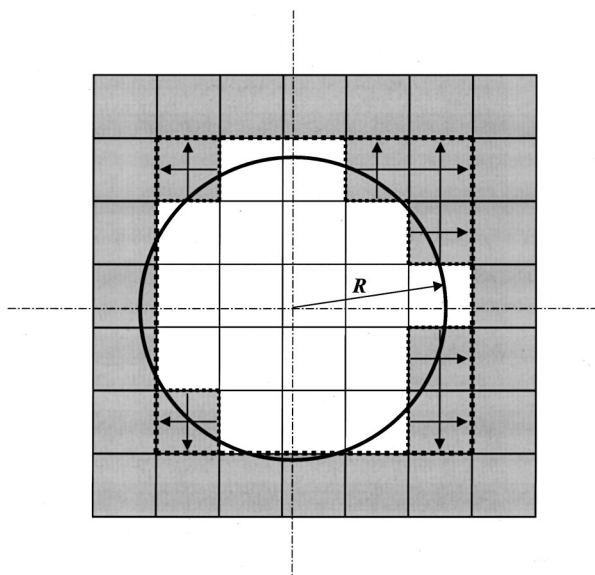


FIG. 2. Perimeter of a circle represented by a digital image. When the pixel size is reduced, the perimeter converges to the perimeter of a square whose size is the diameter of the circle. A 27% increase in perimeter of the circle results when measured within the digital image.

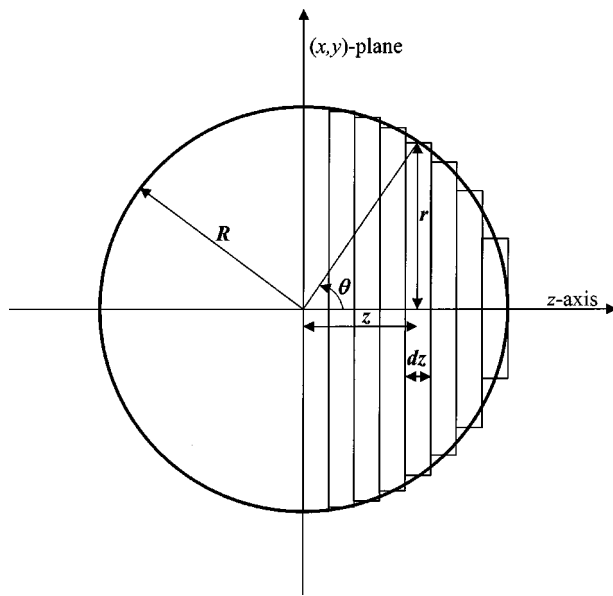


FIG. 3. Sketch of the analytical derivation of the surface area of a voxelized sphere. The sphere is divided into circular slices of thickness  $dz$  and of radius  $r$ . The surface area of the edge of each slice is calculated using the 2D results. The total surface area is obtained by integrating over the entire sphere.

the 3D image. The surface area of the edge of each voxelized disk can be derived from the previous result for the circle by multiplying the perimeter of the disk (within the voxelized image) by its thickness (the voxel size):

$$dS = 8r dz. \quad (2)$$

When the voxel size is reduced to an infinitely small value, the total surface area can be calculated by the integration:

$$S = 2 \int_0^R 8r dz. \quad (3)$$

However, this expression only accounts for the surface area of the edges of the voxelized disks. These edges are perpendicular to the  $x$  axis or the  $y$  axis but never perpendicular to the  $z$  axis; therefore, due to the symmetry of the problem, they account for only two-thirds of the total surface area of the voxelized sphere. The total surface is then obtained by

$$S = 3 \int_0^R 8r dz. \quad (4)$$

Using a variable change,

$$r = R \sin \theta, \quad z = R \cos \theta \Rightarrow dz = -R \sin \theta d\theta. \quad (5)$$

The integration thus becomes

$$S = 24R^2 \int_0^{\pi/2} (\sin \theta)^2 d\theta. \quad (6)$$

The calculation gives the following result:

$$S = 6\pi R^2. \quad (7)$$

Equation (7) shows that reducing the voxel size will make the surface area of a voxelized sphere converge to a value

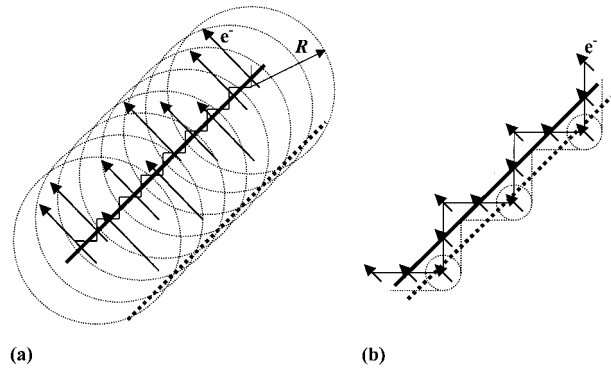


FIG. 4. Schematic showing how the surface-area error within a digital image impacts the absorbed fraction calculation with varying voxel size. In (a) the electron range is larger than the voxel size and in (b) it is smaller.

that is 50% higher than the real surface area of the sphere ( $4\pi R^2$ ). For larger voxel sizes the surface area will be slightly larger or slightly smaller than the convergence value according to the ratio of the voxel size and the sphere radius.

#### D. Measurement of the surface area of a voxelized sphere

In order to check the theoretical result given by Eq. (7), the surface area of the spheres was measured within each simulated image. A computer program was created to perform this task. Its principle is to sweep every voxel of the image and to check if the six adjacent voxels (or less if the voxel is on the edge of the cube) are composed of a different medium. Each time one adjacent voxel is found of a different medium, the surface area of the interface between the current and the adjacent voxel is added to the total surface area. By doing this, each surface is counted twice, and therefore the final result is reduced by a factor of 2 to obtain the true surface area of the voxelized sphere.

#### E. Consequence of an error in surface area on the absorbed fraction calculation

The overestimation of the surface area will affect the result of the Monte Carlo transport code when the particles are emitted close to the boundary of the two media, as each electron will have a greater than normal chance of crossing that boundary. This surface-area effect will vary for different voxel sizes as demonstrated in Fig. 4.

Figure 4(a) demonstrates the situation in which the voxel size is small compared to the electron range. The diagram is in 2D but it can be easily transposed to the 3D situation. The thick solid straight line represents the real boundary between the medium of the radiation source (lower right side of the line), and the medium of the irradiated target (upper left side). The thin solid jagged line represents the same boundary, but as seen within the corresponding digital image. This boundary follows the shape of the rectangular image pixels. The arrows represent electrons (assumed monoenergetic) crossing the boundary. In both situations (the real boundary and the jagged one), electrons crossing the boundary must leave the source at a distance shorter than their range in the

source medium. Therefore, in the real situation, the effective source area from which the electrons can reach the other medium extends from the boundary to the thick dashed straight line, the distance between the two lines being the electron range. In the case of the digital image, the effective source area is more complex, as the boundary is no longer straight. Each dashed circle represents the limit of the effective source area from which the electrons can reach each corner of the image boundary located on the source side of the real interface. The radius  $R$  is equal to the electron range. These circles extend slightly over the thick dashed straight line since their radius is equal to the distance between the two thick lines. The overall limit of the effective source area is the envelope of these circles. One can see in Fig. 4(a) that the source area enclosed between the thin jagged line and the envelope of the circles is nearly identical to the source area enclosed between the two thick lines. Therefore, if the voxel size is small compared to the electron range, the error in interface length introduces little error on the cross-region absorbed fraction calculation since approximately the same number of electrons cross the boundary in the real case as within the digital image.

Figure 4(b) represents the same geometrical features as in Fig. 4(a), but for a voxel size that is larger than the electron range. Only the circles centered at the corners of the thin solid line have been represented, but one can easily understand that the envelope of the effective source area from which the electrons can reach the other medium extends from the solid thin jagged line to the dashed thin line (envelope of the circles). In this case, the two source areas (between the thick lines and between the thin lines) are different. Since the electron range is smaller than the voxel size, the shape of the interface affects the source area from which the electrons can reach the other side. This source area converges to the length of the thin solid line multiplied by the electron range when the voxel size becomes very large compared to the electron range.

The 3D situation is similar and the effective source volume from which the electrons can reach the other side of the boundary is proportional to its surface area when the voxel size is larger than the electron range. Therefore, a 50% overestimation of the surface area overestimates the effective source volume for cross irradiation by 50% as well. Correspondingly, the cross-region absorbed fraction is also overestimated by as much as 50%.

The real boundary in the example problem of Fig. 4 is a straight line; this represents a geometry large in comparison to the electron range. In a smaller relative geometry, the shapes would be more complex but the principle would remain the same.

For the single-sphere models, let us assume that monoenergetic electrons start from the outside of the sphere (the bone trabeculae) and that the absorbed fraction within the sphere (the marrow cavity) is to be calculated. Taking into account the surface-area effect alone, and for a very large voxel sizes, the resulting absorbed fraction is expected to overestimate its exact value by 50% since the electron range is much smaller than the voxel size. By reducing the voxel

## % Error on $\phi$

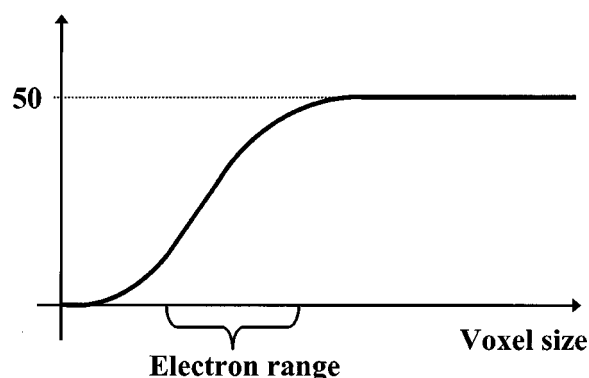


Fig. 5. Expected evolution of the cross-absorbed fraction overestimation for monoenergetic electrons as a function of the voxel size.

size, the voxel dimensions will approach the electron range and thus the absorbed fraction would become closer to its exact value. If the voxel size is chosen very small, the results should converge. This scenario is shown in Fig. 5. The voxel size at which the convergence appears should be around, or at least function of, the electron range in the source region.

## F. Electron transport simulations

The next step in the study is to calculate the absorbed fractions of energy and to analyze their evolution with the voxel size. For this, particle transport calculations were performed using the EGS4-PRESTA code. At the time of this study, the EGSNRC code had not yet been introduced. Nevertheless, the resulting transport improvements over EGS4-PRESTA will not have consequences on the results of the current study, as the problem related here is a purely one of geometry. Two transport simulations were performed. One for a uniform monoenergetic electron source located within the sphere (e.g., marrow source) and a second for a uniform monoenergetic electron source located outside the sphere (e.g., bone source) but within the limits of the bone cube. For each simulation, six electron energies were used. As the surface-area effect only influences the calculation for low-energy electrons,<sup>44</sup> the maximum energy was set to 320 keV. The minimum energy was set to 10 keV. For each electron energy and for both source regions, one set of EGS4 runs was performed for each single-sphere model. Each set represents one simulation within the exact single-sphere model and one simulation within each 3D image (each voxel size shown in Table II). Therefore, two different EGS4 user codes were developed: a “reference code” for the exact sphere model, using the equation of the sphere delineating the marrow cavity boundary, and an “image code” for the different segmented images, using equations of planes separating the voxels. The “reference code” was executed for each model and for each electron energy. The “image code” was executed for each model, for each electron energy, and for each image resolution.

The transport parameters used by EGS4 were the same in both codes. The characteristics of the bone and marrow me-

TABLE III. List of electron energies used in the study. The total number of histories per energy is equal to the number of runs multiplied by the number of histories per run.

Electron energy (keV)	Number of runs	Histories per run for source inside the sphere	Histories per run for source outside the sphere
10	100	120 000	300 000
20	100	50 000	125 000
40	100	10 000	25 000
80	100	4000	10 000
160	100	1600	4000
320	100	800	2000

dia were identical to those used for the study of the mathematical trabecular bone model.<sup>44</sup> For the PRESTA extension, the ESTEPE parameter was set to 0.05. For each execution, absorbed fractions of energy were estimated for targets inside the sphere, outside the sphere but inside the cube, and outside the cube (energy lost for this study). Only the cross-absorbed fraction results are shown and analyzed in this work.

The absorbed fractions calculated with the “image code” were compared to the absorbed fractions calculated with the “reference code.” The absorbed fraction relative error  $\Delta r_\phi$  produced by the overestimation of the boundary surface area was then evaluated using the following expression:

$$\Delta r_\phi = \left( \frac{\phi_{\text{ima}} - \phi_{\text{ref}}}{\phi_{\text{ref}}} \right) \times 100\%, \quad (8)$$

where  $\phi_{\text{ima}}$  is the absorbed fraction calculated using the “image code” and  $\phi_{\text{ref}}$  is the absorbed fraction calculated using the “reference code.”

### G. Statistical analysis

Combining all parameters described previously, a total of 1764 EGS4 simulations were performed. In order to minimize the calculation time, a statistical analysis was performed prior to the EGS4 simulations. Instead of one execution of  $N$  histories, 100 runs were performed. For each run, only one-hundredth of  $N$  histories were used. This allows calculating a mean and a standard deviation within the sample of 100 runs. The standard deviation of the mean can also be estimated, as well as a 95% confidence interval assuming a normal distribution of the mean. As it is not known whether or not the distribution of the absorbed fraction follows a normal distribution, the later assumption is verified through application of the central limit theorem. This explains the large sample (100 runs in this case) used for this analysis. The number of histories was chosen so that the 95% confidence interval for the mean was reduced to about  $\pm 2\%$  for each absorbed fraction calculated. As the accuracy of the result varies mostly with the electron energy and the source region, a different number of histories was set for each situation in order to reach the 2% goal and to minimize the calculation time. Table III shows the electron energies used and the number of histories per run for both types of sources.

Note that this 95% confidence interval is representative of the statistical fluctuation of the results due to the randomness

of the Monte Carlo method. It does not represent the accuracy of the technique used. It signifies that another experiment using the same Monte Carlo transport code and the same experimental conditions would have a 95% chance to find a result within the confidence interval. The purpose of this work is not to assess the accuracy of the dosimetry technique, but to quantify the error due to the surface area overestimate. In order to calculate the 95% confidence interval for the relative error, the error propagation technique was used. According to the theory,<sup>46,47</sup> the standard deviation of a function  $f(x,y)$  is given by

$$\sigma_f = \sqrt{\left( \frac{\partial f}{\partial x} \right)^2 \sigma_x^2 + \left( \frac{\partial f}{\partial y} \right)^2 \sigma_y^2}. \quad (9)$$

In our situation, using Eq. (8) to calculate the partial derivatives, the expression becomes

$$\sigma_{\Delta r_\phi} = \frac{\sqrt{\phi_{\text{ref}}^2 \sigma_{\phi_{\text{ima}}}^2 + \phi_{\text{ima}}^2 \sigma_{\phi_{\text{ref}}}^2}}{\phi_{\text{ref}}^2}. \quad (10)$$

In Eq. (10),  $\sigma_{\phi_{\text{ref}}}$  and  $\sigma_{\phi_{\text{ima}}}$  are the standard deviations of the mean calculated with  $N=100$  runs of, respectively, the “reference code” and the “image code” using the relation

$$\sigma_\phi = \sqrt{\frac{\sum_{i=1}^N (\phi_i - \bar{\phi})^2}{N(N-1)}}. \quad (11)$$

The 95% confidence interval is therefore obtained by

$$\text{Err}_{95\%} = \pm 1.96 \frac{\sqrt{\phi_{\text{ref}}^2 \sigma_{\phi_{\text{ima}}}^2 + \phi_{\text{ima}}^2 \sigma_{\phi_{\text{ref}}}^2}}{\phi_{\text{ref}}^2}. \quad (12)$$

## III. RESULTS AND DISCUSSION

The results from the eight single-sphere models are quite consistent. Therefore, only four models are shown in the following. The models chosen are 1400, 0728, 0350, and 0069.

### A. Volume fraction occupied by the spheres within the segmented images

The volume fraction occupied by the spheres within the segmented images is compared with the exact value in Fig. 6 for each model. In this figure, the horizontal solid lines represent the exact volume fraction of the spheres, with values given in column 6 of Table I. For each model, the volume fraction converges toward its exact value as the voxel size is



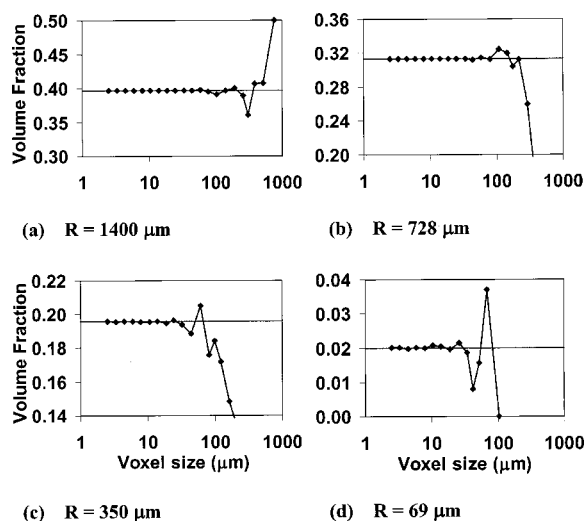


FIG. 6. Volume fraction occupied by the sphere within the segmented image as a function of the voxel size. The horizontal solid line is the volume fraction occupied by the real sphere. The four single-sphere models represented are (a) 1400, (b) 0728, (c) 0350, and (d) 0069.

reduced. The convergence occurs around a voxel size that decreases as the radius of the marrow sphere decreases.

The study of the mathematical trabecular bone model<sup>44</sup> showed that the error on the volume fraction at large voxel sizes, referred to as the volume-fraction effect, was not a concern for dosimetry calculations since it occurs only above 300  $\mu\text{m}$  in a typical bone sample. Therefore, in the remainder of this study, we focus only on voxel sizes small enough so that the surface-area effect can be studied in isolation.

## B. Surface-area of the 3D segmented images

The surface areas calculated within the segmented images are compared with their exact values in Fig. 7. In Fig. 7, the

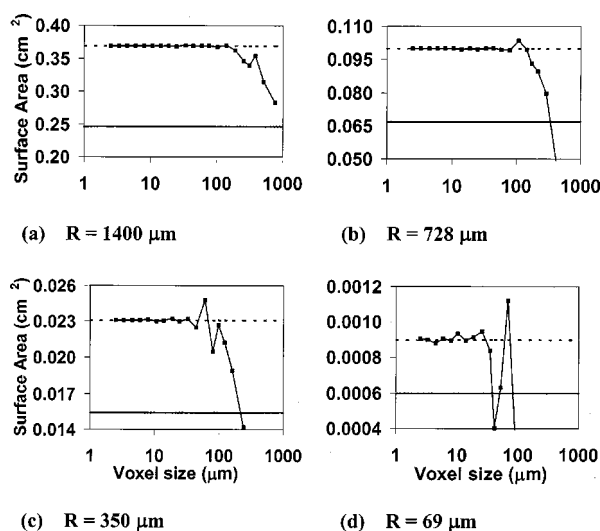


FIG. 7. Surface area of the segmented spheres, as a function of the voxel size. The horizontal solid line is the exact surface area of the sphere. The horizontal dashed line is located at 1.5 times the exact value. The four single-sphere models represented are (a) 1400, (b) 0728, (c) 0350, and (d) 0069.

horizontal solid lines represent the exact surface areas of the marrow spheres whose values are given in column 4 of Table I. The dashed lines are at 1.5 times the exact values. These results are in excellent agreement with predicted values calculated in Sec. II C. Furthermore, the surface area is expected to oscillate around a convergence value. It can be larger or smaller than the convergence value according to the ratio between the voxel size and the sphere radius. These oscillations are particularly evident for the small spheres; for the larger ones, they are barely visible, but still present. At large voxel sizes, the oscillations disappear for all spheres since the surface area effect is overwhelmed by the volume fraction effect. For very large voxel sizes, the surface area drops to zero as the image approaches 100% osseous tissue following image segmentation.

## C. Absorbed fractions within the 3D segmented images

The next step was to calculate the absorbed fraction of energy deposited by electrons within the different models. In this section, only the cross-absorbed fractions are considered since the self-absorbed fractions are reasonably accurate even at small voxel sizes.<sup>44</sup> The results are presented in Fig. 8 for electron sources in bone irradiating marrow, and in Fig. 9 for electron sources in the marrow irradiating bone. In each figure, the four selected models are shown: Figs. 8(a) and 9(a) are for model 1400, Figs. 8(b) and 9(b) are for model 0728, Figs. 8(c) and 9(c) are for model 0350, and Figs. 8(d) and 9(d) are for model 0069. For each graph, curves are shown which represent the relative error in the cross-absorbed fraction given by Eq. (8) as a function of the voxel size and electron energy. The error bars show the 95% confidence intervals calculated by Eq. (12). These curves are to be compared with the expected results shown schematically in Fig. 5.

First, for voxel sizes larger than the resolution at which the volume fraction converges, the results cannot be interpreted by the surface-area error alone since it is overwhelmed and largely influenced by the volume fraction. This is why, at these voxel sizes, the absorbed fraction can be overestimated or underestimated, depending upon the volume fraction of the segmented sphere. At this resolution, one can see that the shapes of the absorbed-fraction curves follow more or less the shapes of the volume fraction curves.

Second, for a voxel size small enough so as to minimize the volume-fraction effect, the surface-area effect is visible in each model as predicted in Sec. II E. The 50% overestimate of the surface area leads to a 50% overestimate of the cross-absorbed fraction down to a voxel size that depends on the electron energy. Below this voxel size, the absorbed fraction converges to its exact value. This convergence is only visible at high energies; at very low-energy electron sources (e.g., 10 and 20 keV), the shape of the absorbed-fraction curve indicates that a similar effect would occur at a voxel size below the range used in the study. These results are in strong agreement with Fig. 5.

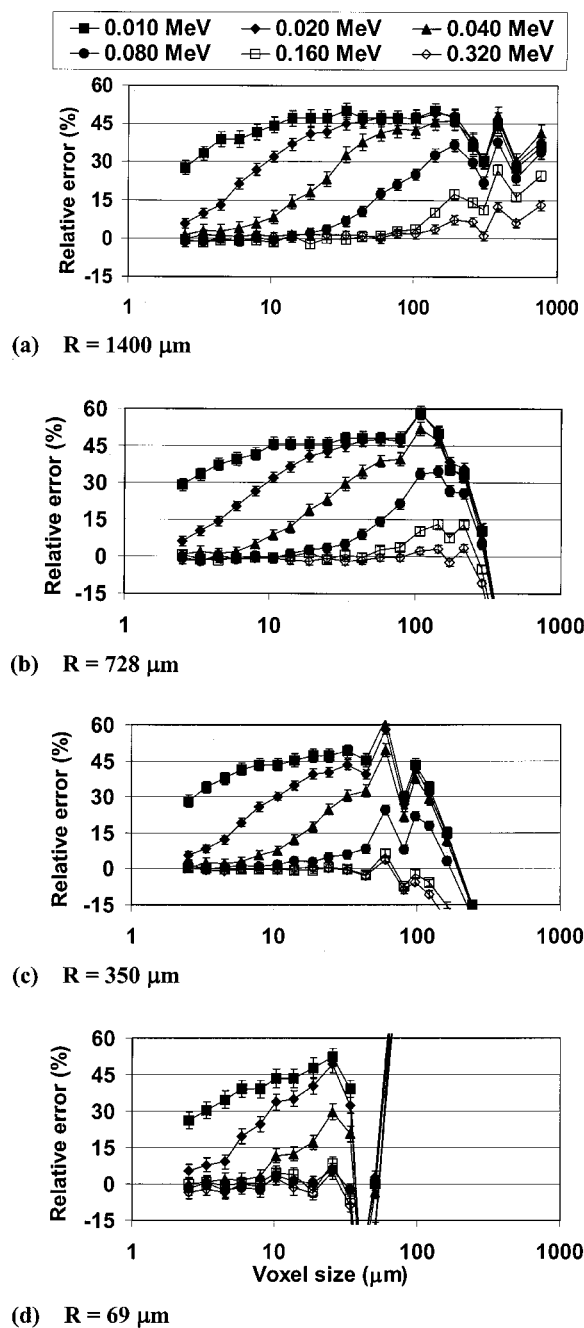


FIG. 8. Relative error made while calculating the fraction of energy deposited inside the sphere for electrons emitted outside the sphere (bone source irradiating marrow). The four single-sphere models represented are (a) 1400, (b) 0728, (c) 0350, and (d) 0069.

Third, the resolution at which the absorbed fraction starts to converge toward the exact value can be compared with the electron range as shown in Table IV (data from ICRU Publication 37<sup>48</sup>). At electron energies from 20 to 80 keV, the electron range is equal to the voxel size that corresponds to a relative error of  $\sim 25\%$  (i.e., the middle of the convergence slope). For the 10 keV curves, the voxel size is not extended to a value small enough to show the same consequence, but an extrapolation of these curves can be easily made. At

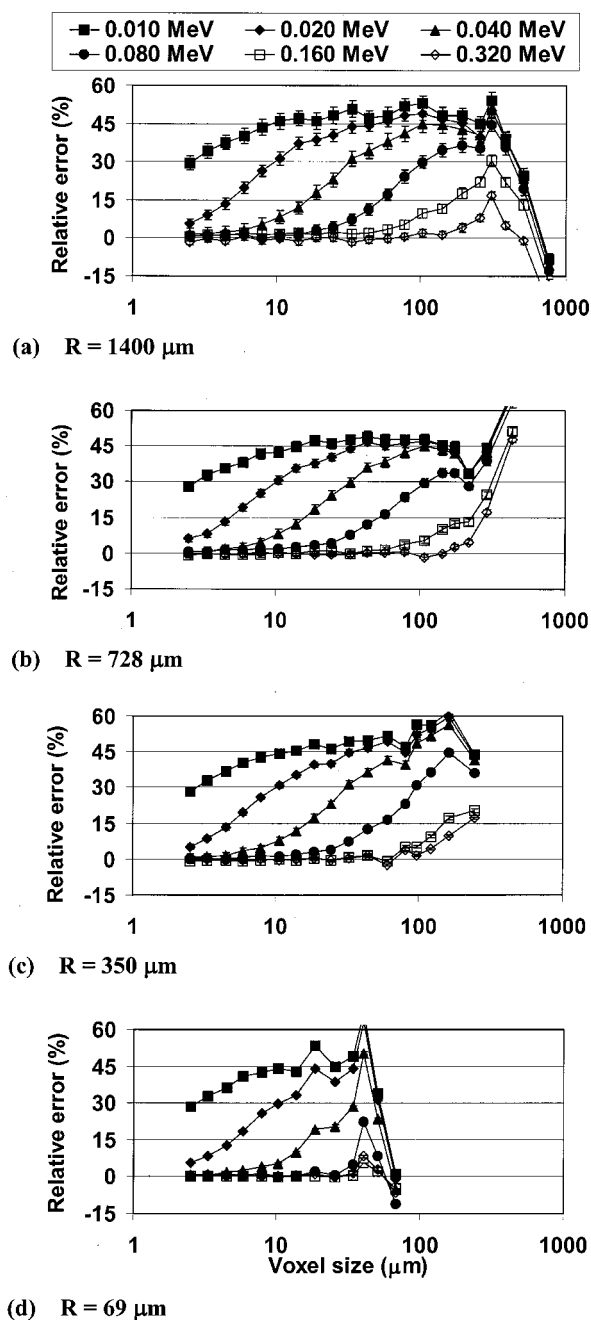


FIG. 9. Relative error made while calculating the fraction of energy deposited outside the sphere for electrons emitted within the sphere (marrow source irradiating bone). The four single-sphere models represented are (a) 1400, (b) 0728, (c) 0350, and (d) 0069.

higher electron energies (160 and 320 keV curves), the convergence slope falls above the volume-fraction convergence value. Once again, the convergence slope can be deduced from the lower part of the curves, and the extrapolated shapes would show a convergence slope at a voxel size close to the electron range.

Finally, one can see that, at voxel sizes that are not affected by the volume fraction effect, the sphere radius does not change the shape of the curves. The surface area effect

TABLE IV. Electron ranges in bone marrow (density =  $1.03 \text{ g cm}^{-3}$ ) and cortical bone (density =  $1.92 \text{ g cm}^{-3}$ ). The values have been interpolated from ICRU Publication 37 (Ref. 48), using cortical bone and water (corrected for density) for bone marrow.

Electron energy (keV)	CSDA range in bone marrow ( $\mu\text{m}$ )	CSDA range in cortical bone ( $\mu\text{m}$ )
10	2.4	1.4
20	8.3	4.9
40	28	16
80	95	55
160	300	180
320	900	520

depends only on the ratio between the electron range and the voxel size, as predicted in Sec. II E.

#### IV. CONCLUSION

The surface area effect resulting from the segmentation of an object within its 3D digital image has been investigated using single-sphere models of trabecular bone-marrow cavities. It has been shown, both analytically and experimentally, that a consequence of the image segmentation is an overestimation of the interface surface area. This overestimate, identified as a surface-area effect, is a result of the rectangular shape of the voxels that constitute the image and cannot be reduced by improved resolution. In the case of single spheres, the overestimate is as high as 50%. This finding is consistent with the studies of Rajon *et al.* where a similar overestimate of bone-marrow interface area was found in a mathematical model of trabecular bone.<sup>44</sup>

The dosimetry consequence of the surface-area effect is an overestimate of the absorbed fraction by electrons cross-irradiating a region adjacent to the source region (bone source irradiating marrow, for example). At a voxel size larger than the electron range, this overestimate is equal to the overestimate of the surface area (50% for spherical objects). As the voxel size is reduced, the error decreases and becomes insignificant when the voxel size falls below the electron range. For high-energy electrons, this effect is inconsequential since the electron range is significantly larger than the voxel size used to image trabecular bone samples. For electron energies below 100 keV, however, the effect is significant to a voxel size down to a value on the order of a few micrometers. With typical resolutions used in NMR microscopy (from 60 to  $100 \mu\text{m}$ ), and for very low-energy beta emitters (e.g.,  $^{117\text{m}}\text{Sm}$  and  $^{33}\text{P}$ ), the dose calculation using these absorbed fractions leads to a 25% overestimate within the mathematical model of trabecular bone.<sup>44</sup> This mathematical model was designed with dosimetry features as close as possible to those of a real trabecular bone sample, and thus the same consequence is expected within NMR images of real samples.

As shown in Fig. 5, the problem can be incrementally solved by improving the image resolution. Figures 8 and 9 shows that for low-energy electrons, let us say 40 keV, the resolution needs to be pushed downward to  $\sim 5 \mu\text{m}$  in order

to achieve a close estimate of the cross-dose. This resolution is  $\sim 10$  times better than what is currently performed in NMR microscopy of trabecular bone,<sup>49</sup> and  $\sim 6$  times better than available with microCT systems.<sup>50</sup> Increased resolution of the NMR microscopy images are possible via improvements in the signal-to-noise ratio of the NMR system acquisition via higher field strengths (e.g., 20 T) and/or longer imaging times. Compromises occur, however, in that one must contend with susceptibility artifacts at the bone-marrow interface at higher fields, and longer imaging sessions can become cost prohibitive. In addition, as the images become larger with decreasing voxel size, computer storage can potentially be an issue.

Nevertheless, other solutions to the problem may be sought. One such solution would be to perform an interpolation of the gray-level values of the original NMR image to calculate a polygonal isosurface that would represent the bone-marrow interface. In this manner, image voxels at the interface would encompass one or more polygons separating the marrow tissues from the osseous bone tissue. The exact positions and relative angles between polygons would be a function of both the relative gray level of the interface voxels and the resolution of the image (i.e., voxel size). The resulting collection of polygons would thus permit a more smooth representation of the true bone-marrow interface surface and would thus better represent the true surface area. Such a polygonal isosurface has already been used with trabecular bone microstructure<sup>51</sup> and its construction is based on the Marching Cube algorithm developed during the 1980s by Lorensen and Cline.<sup>52</sup> In this algorithm, the resulting isosurface is only made of triangles that ensure that each piece of the surface can be modeled with equations of planes. Through the application of this technique, previous problems identified in either the assessment of bone and marrow chord-length distributions,<sup>42</sup> as well as absorbed fractions for cross-irradiation by low-energy electrons<sup>44</sup> would be significantly reduced from those found using voxelized geometries. The storage capacity of the computer would still remain a major concern, since the number of triangles would be on the same order of the number of voxels, but the image resolution no longer needs to be tremendously improved, and may even be reduced if the voxel effects are shown to be significantly reduced. Research in applying this technique to NMR microscopy images of trabecular bone, and coupling the isosurface to radiation transport codes, is ongoing.

#### ACKNOWLEDGMENT

This work was supported by U.S. DOE Nuclear Engineering Education Research (NEER) Grant No. DE-FG07-ID13764 with the University of Florida.

<sup>a)</sup> Author to whom correspondence should be addressed. Electronic mail: wbolch@ufl.edu

<sup>1</sup> G. Sgouros, "Bone marrow dosimetry for radioimmunotherapy: Theoretical considerations," *J. Nucl. Med.* **34**, 689–694 (1993).

<sup>2</sup> G. Sgouros, M. Stabin, Y. Erdi, G. Akabani, C. Kwok, A. B. Brill, and B. Wessels, "Red marrow dosimetry for radiolabeled antibodies that bind to marrow, bone, or blood components," *Med. Phys.* **27**, 2150–2164 (2000).

- <sup>3</sup> A. Brodsky, *Review of Radiation Risks and Uranium Toxicity with Applications to Decisions Associated with Decommissioning Clean-Up Criteria* (RAS, Hebron, CT, 1996).
- <sup>4</sup> J. A. Siegel, B. W. Wessels, and E. E. Watson, "Bone marrow dosimetry and toxicity for radioimmunotherapy," *Antibody, Immunoconjugates, Radiopharm.* **3**, 213–233 (1990).
- <sup>5</sup> L. G. Bouchet, W. E. Bolch, S. M. Goddu, R. W. Howell, and D. V. Rao, "Considerations in the selection of radiopharmaceuticals for palliation of bone pain from metastatic osseous lesions," *J. Nucl. Med.* **41**, 682–687 (2000).
- <sup>6</sup> C. B. Clayman, *The Human Body: An Illustrated Guide to its Structure, Function, and Disorders* (Dorling Kindersley, London, 1995).
- <sup>7</sup> E. N. Marieb, *Human Anatomy and Physiology* (Benjamin/Cummings, Menlo Park, CA, 1998).
- <sup>8</sup> F. W. Spiers, "Dose to trabecular bone from internal beta-emitters," in *First International Congress of Radiation Protection*, edited by W. S. Snyder (Pergamon, Rome, 1966), pp. 165–172.
- <sup>9</sup> A. H. Beddoe, "A quantitative study of the structure of mammalian bone," *J. Anat.* **122**, 190 (1976).
- <sup>10</sup> A. H. Beddoe, P. J. Darley, and F. W. Spiers, "Measurements of trabecular bone structure in man," *Phys. Med. Biol.* **21**, 589–607 (1976).
- <sup>11</sup> F. W. Spiers, A. H. Beddoe, and J. R. Whitwell, "Mean skeletal dose factors for beta-particle emitters in human bone 1. Volume-seeking radionuclides," *Br. J. Radiol.* **51**, 622–627 (1978).
- <sup>12</sup> F. W. Spiers, J. R. Whitwell, and A. H. Beddoe, "Calculated dose factors for the radiosensitive tissues in bone irradiated by surface-deposited radionuclides," *Phys. Med. Biol.* **23**, 481–494 (1978).
- <sup>13</sup> J. R. Whitwell, "Theoretical investigations of energy loss by ionizing particles in bone," thesis, Department of Medical Physics, University of Leeds, Leeds, UK, 1973, 268 pp.
- <sup>14</sup> J. R. Whitwell and F. W. Spiers, "Calculated beta-ray dose factors for trabecular bone," *Phys. Med. Biol.* **21**, 16–38 (1976).
- <sup>15</sup> W. S. Snyder, M. R. Ford, G. G. Warner, and S. B. Watson, "A tabulation of dose equivalent per microcurie-day for source and target organs of an adult for various radionuclides," ORNL/TM-5000, Oak Ridge National Laboratory, Oak Ridge, TN, 1974.
- <sup>16</sup> W. S. Snyder, M. R. Ford, G. G. Warner, and S. B. Watson, "S," *Absorbed Dose per Unit Cumulated Activity for Selected Radionuclides and Organs* (Society of Nuclear Medicine, New York, 1975).
- <sup>17</sup> L. G. Bouchet, W. E. Bolch, R. W. Howell, and D. V. Rao, "S values for radionuclides localized within the skeleton," *J. Nucl. Med.* **41**, 189–212 (2000).
- <sup>18</sup> L. G. Bouchet, D. W. Jokisch, and W. E. Bolch, "A three-dimensional transport model for determining absorbed fractions of energy for electrons in trabecular bone," *J. Nucl. Med.* **40**, 1947–1966 (1999).
- <sup>19</sup> M. G. Stabin, "MIRDose: Personal computer software for internal dose assessment in nuclear medicine," *J. Nucl. Med.* **37**, 538–546 (1996).
- <sup>20</sup> K. F. Eckerman, "Aspects of the dosimetry of radionuclides within the skeleton with particular emphasis on the active marrow," in *Proceedings of the Fourth International Radiopharmaceutical Dosimetry Symposium*, edited by A. T. Sch Lafke-Stelson and E. E. Watson (ORAU, Oak Ridge, TN, 1985), pp. 514–534.
- <sup>21</sup> K. F. Eckerman and M. G. Stabin, "Electron absorbed fractions and dose conversion factors for marrow and bone by skeletal regions," *Health Phys.* **78**, 199–214 (2000).
- <sup>22</sup> X. Ouyang, K. Selby, T. F. Lang, K. Engelke, C. Klifa, B. Fan, F. Zucconi, G. Hottya, M. Chen, S. Majumdar, and H. K. Genant, "High resolution magnetic resonance imaging of the calcaneus: Age-related changes in trabecular structure and comparison with dual x-ray absorptiometry measurements," *Calcif. Tissue Int.* **60**, 139–147 (1997).
- <sup>23</sup> B. D. Snyder, S. Piazza, W. T. Edwards, and W. C. Hayes, "Role of trabecular morphology in the etiology of age-related vertebral fractures," *Calcif. Tissue Int.* **53**, S14–S22 (1993).
- <sup>24</sup> L. Mosekilde, "Age-related changes in vertebral trabecular architecture assessed by a new method," *Bone (N.Y.)* **9**, 247–250 (1986).
- <sup>25</sup> L. Mosekilde, "Sex differences in age-related loss of vertebral trabecular bone mass and structure-biomechanical consequences," *Bone (N.Y.)* **10**, 425–432 (1989).
- <sup>26</sup> H. G. Bone, D. D. Cody, and E. M. Monsell, "Application of quantitative computed tomography to Paget's Disease of bone," *Semin Arthritis Rheum.* **23**, 244–247 (1994).
- <sup>27</sup> D. D. Cody, M. J. Flynn, and D. S. Vickers, "A technique for measuring regional bone mineral density (rBMD) in human lumbar vertebral bodies," *Med. Phys.* **16**, 766–772 (1989).
- <sup>28</sup> D. D. Cody, S. A. Goldstein, M. J. Flynn, and E. B. Brown, "Correlations between vertebral regional bone mineral density (rBMD) and whole bone fracture load," *Spine* **16**, 146–154 (1991).
- <sup>29</sup> M. J. Flynn and D. D. Cody, "The assessment of vertebral bone macroarchitecture with x-ray computed tomography," *Calcif. Tissue Int.* **53**, S170–S175 (1993).
- <sup>30</sup> S. Grampp, S. Majumdar, M. Jergas, D. C. Newitt, P. Lang, and H. K. Genant, "Distal radius: *In vivo* assessment with quantitative MR imaging, peripheral quantitative CT, and dual x-ray absorptiometry," *Radiology* **198**, 213–218 (1996).
- <sup>31</sup> M. Kleerekoper, D. A. Nelson, M. J. Flynn, A. S. Pawluszka, G. Jacobsen, and E. L. Peterson, "Comparison of radiographic absorptiometry with dual-energy x-ray absorptiometry and quantitative computed tomography in normal older white and black women," *J. Bone Miner. Res.* **9**, 1745–1749 (1994).
- <sup>32</sup> M. Kleerekoper, D. A. Nelson, E. L. Peterson, M. J. Flynn, A. S. Pawluszka, G. Jacobsen, and P. Wilson, "Reference data for bone mass, calciotropic hormones, and biochemical markers of bone remodeling in older (55–75) postmenopausal white and black women," *J. Bone Miner. Res.* **9**, 1267–1276 (1994).
- <sup>33</sup> T. M. Link, S. Majumdar, W. Konermann, N. Meier, J. C. Lin, D. Newitt, X. Ouyang, P. E. Peters, and H. K. Genant, "Texture analysis of direct magnification radiographs of vertebral specimens: Correlation with bone mineral density and biomechanical properties," *Acad. Radiol.* **4**, 167–176 (1997).
- <sup>34</sup> T. M. Link, S. Majumdar, J. C. Lin, P. Augat, R. G. Gould, D. Newitt, X. Ouyang, T. F. Lang, A. Mathur, and H. K. Genant, "Assessment of trabecular structure using high resolution CT images and texture analysis," *J. Comput. Assist. Tomogr.* **22**, 15–24 (1998).
- <sup>35</sup> T. M. Link, S. Majumdar, J. C. Lin, D. Newitt, P. Augat, X. Ouyang, A. Mathur, and H. K. Genant, "A comparative study of trabecular bone properties in the spine and femur using high resolution MRI and CT," *J. Bone Miner. Res.* **13**, 122–132 (1998).
- <sup>36</sup> F. Chevalier, A. M. Laval-Jeantet, M. Laval-Jeantet, and C. Bergot, "CT image analysis of the vertebral trabecular network *in vivo*," *Calcif. Tissue Int.* **51**, 8–13 (1992).
- <sup>37</sup> E. P. Durand and P. Rueggsegger, "High-contrast resolution of CT images for bone structure analysis," *Med. Phys.* **19**, 569–573 (1992).
- <sup>38</sup> J. L. Kuhn, S. A. Goldstein, L. A. Feldkamp, R. W. Goulet, and G. Jesion, "Evaluation of a microcomputed tomography system to study trabecular bone structure," *J. Orthop. Res.* **8**, 833–842 (1990).
- <sup>39</sup> S. Majumdar, H. K. Genant, S. Grampp, D. C. Newitt, V. H. Truong, J. C. Lin, and A. Mathur, "Correlation of trabecular bone structure with age, bone mineral density, and osteoporotic status: *In vivo* studies in the distal radius using high-resolution magnetic resonance imaging," *J. Bone Miner. Res.* **12**, 111–118 (1997).
- <sup>40</sup> R. Müller, R. Hildebrand, H. J. Häuselmann, and P. Rueggsegger, "In vivo reproducibility of three-dimensional structural properties of noninvasive bone biopsies using 3D-pQCT," *J. Bone Miner. Res.* **11**, 1745–1750 (1996).
- <sup>41</sup> D. W. Jokisch, P. W. Patton, B. A. Inglis, L. G. Bouchet, D. A. Rajon, J. Rifkin, and W. E. Bolch, "NMR microscopy of trabecular bone and its role in skeletal dosimetry," *Health Phys.* **75**, 584–596 (1998).
- <sup>42</sup> D. W. Jokisch, P. W. Patton, D. A. Rajon, B. A. Inglis, and W. E. Bolch, "Chord distributions across 3D digital images of a human thoracic vertebra," *Med. Phys.* **28**, 1493–1504 (2001).
- <sup>43</sup> D. W. Jokisch, L. G. Bouchet, P. W. Patton, D. A. Rajon, and W. E. Bolch, "Beta-particle dosimetry of the trabecular skeleton using Monte Carlo transport within 3D digital images," *Med. Phys.* **28**, 1505–1518 (2001).
- <sup>44</sup> D. A. Rajon, D. W. Jokisch, P. W. Patton, A. P. Shah, and W. E. Bolch, "Voxel size effects in 3D NMR microscopy performed for trabecular bone dosimetry," *Med. Phys.* **27**, 2624–2635 (2000).
- <sup>45</sup> J. Peter, M. P. Tornai, and R. J. Jaszczek, "Analytical versus voxelized phantom representation for Monte Carlo simulation in radiological imaging," *IEEE Trans. Med. Imaging* **19**, 556–564 (2000).
- <sup>46</sup> G. F. Knoll, *Radiation Detection and Measurement* (Wiley, New York, 1989).
- <sup>47</sup> J. E. Turner, *Atoms, Radiation, and Radiation Protection* (Wiley, New York, 1995).
- <sup>48</sup> ICRU, "Stopping powers for electrons and positrons," Report No. 37,



International Commission on Radiation Units and Measurements, Bethesda, MD, 1984.

- <sup>49</sup>P. W. Patton, D. W. Jokisch, D. A. Rajon, A. P. Shah, S. L. Myers, and W. E. Bolch, "Skeletal dosimetry via NMR microscopy: Investigations of sample reproducibility and signal source," *Health Phys.* **82**, 316–326 (2002).
- <sup>50</sup>P. Rüegsegger, B. Koller, and R. Müller, "A microtomographic system for the nondestructive evaluation of bone architecture," *Calcif. Tissue Int.* **58**, 24–29 (1996).
- <sup>51</sup>R. Müller, T. Hildebrand, and P. Rüegsegger, "Non-invasive bone biopsy: A new method to analyze and display the three-dimensional structure of trabecular bone," *Phys. Med. Biol.* **39**, 145–164 (1994).
- <sup>52</sup>W. E. Lorensen and H. E. Cline, "Marching cubes: A high-resolution 3D surface construction algorithm," *Comput. Graph.* **21**, 163–169 (1987).